

ExoMiner++ 2.0: Vetting TESS Full-Frame Image Transit Signals

MIGUEL J. S. MARTINHO,^{1,2} HAMED VALIZADEGAN,^{1,2} JON M. JENKINS,² DOUGLAS A. CALDWELL,^{3,2}
 JOSEPH D. TWICKEN,^{3,2} BEN TOFFLEMIRE,^{3,2} AND MARZIYE JAFARIYAZANI^{3,2}

¹*KBR, Inc., Mountain View, CA 94043, USA*

²*NASA Ames Research Center (NASA ARC), Moffett Field, CA 94035, USA*

³*The SETI Institute, Mountain View, CA 94043, USA*

Submitted to AJ

ABSTRACT

The *Transiting Exoplanet Survey Satellite* (TESS) Full-Frame Images (FFIs) provide photometric time series for millions of stars, enabling transit searches beyond the limited set of pre-selected 2-minute targets. However, FFIs present additional challenges for transit identification and vetting. In this work, we apply **ExoMiner++** 2.0, an adaptation of the **ExoMiner++** framework originally developed for TESS 2-minute data, to FFI light curves. The model is used to perform large-scale planet versus non-planet classification of Threshold Crossing Events across the sectors analyzed in this study. We construct a uniform vetting catalog of all evaluated signals and assess model performance under different observing conditions. We find that **ExoMiner++** 2.0 generalizes effectively to the FFI domain, providing robust discrimination between planetary signals, astrophysical false positives, and instrumental artifacts despite the limitations inherent to longer cadence data. This work extends the applicability of **ExoMiner++** to the full TESS dataset and supports future population studies and follow-up prioritization.

1. INTRODUCTION

The *Transiting Exoplanet Survey Satellite* (TESS; Ricker et al. 2015) mission has conducted a high-precision and wide photometric survey of the sky over the past seven years and unearthed more than 7,500 planet candidates while enabling the confirmation of more than six hundred new planets. Now into its third Extended Mission (EM3), TESS continues to expand its sky survey through a series of 27-day observation cycles, each covering a $24^\circ \times 96^\circ$ field of view. The observatory collects data using mainly two different modes: 2-minute sampling of up to 20,000 targets per sector and full-frame images (FFI).⁴ For the Prime Mission, the FFI cadence was set to 30 minutes, decreasing to 10 minutes for the First Extended Mission, and to 200 seconds for the following EM2 and EM3. By reducing the cadence for FFI data, the extended missions provide increased sensitivity to short duration transits for more targets and

enable the study of transient stellar events. The TESS Science Processing Operations Center (SPOC; Jenkins et al. 2016) pipeline has been used since the start of the TESS Mission to process 2-minute data to generate data products that include target pixel and light curve files for the different sectors, and the results of transiting planet searches that yield catalogs of Threshold Crossing Events (TCEs), periodic dimming events that might be consistent with planetary transits. The SPOC also produces reports and time series for TCEs that can be used towards vetting and validation efforts. For FFI data, the SPOC pipeline has been used to calibrate FFIs and assign world-coordinate system information to the FFI data delivered to the Mikulski Archive for Space Telescopes⁵ (MAST). Starting with Year 2, the SPOC began processing 30-min targets selected from the FFIs to create calibrated target pixel files and light curves for up to 160,000 targets per sector in the TESS Northern hemisphere, and has continued to do so, with results released up to Year 6 (as of 11 December 2025, through Sector 78). Furthermore, since Sector 36 (Year 3), the SPOC has been running transiting planet searches on the hundreds of thousands of targets selected, yielding

Corresponding author: Hamed Valizadegan
 hamed.valizadegan@nasa.gov

⁴ Target pixel files and light curves are generated for up to 3000 20-second targets per sector since sector 27, but these are not searched for transiting planet signatures. All 20-second targets are also observed at the 2-minute cadence.

⁵ <https://archive.stsci.edu/>

Data Validation (DV; Twicken et al. 2018; Li et al. 2019) products similar to those created for the 2-minute cadence data (for those targets with at least one detected TCE). All of these data products have been delivered to MAST as High-Level Science Products⁶ (HLSP) for FFI targets from Sectors 36 onwards (Caldwell et al. 2020).

The FFI transit searches on a larger population of target stars increase significantly the number of transiting signals that have been detected by data processing pipelines such as SPOC for the TESS Mission. The vast volumes of TCEs produced by these pipelines require vetting systems that are automated, scalable, and capable of vetting faint transit signals with a minimal false positive rate. As demonstrated by the previous works (Shallue & Vanderburg 2018; Armstrong et al. 2020; Valizadegan et al. 2022, 2023, 2025), machine learning methods are particularly well suited for these requirements, as they can identify patterns in a data-driven manner to efficiently vet hundreds of thousands of transiting signals. This allows the exoplanet community to focus their time and resources on a smaller set of candidates by excluding false positives from the initial population generated by transit search runs.

In this work, we build upon our previous efforts in vetting TESS SPOC 2-minute TCEs (Valizadegan et al. 2025), and extend these efforts to the FFI planet searches. More concretely, we present our methodology for vetting TCEs generated from SPOC planet search runs conducted on FFI data. We improve the architecture of `ExoMiner++`, the deep learning model used in (Valizadegan et al. 2025), and train this model for finding planet candidates among the hundreds of thousands of these FFI transiting events, with the goal of providing catalogs that enable focused follow-up observation efforts in a smaller and cleaner set of candidates. These catalogs significantly speed up the exoplanet community’s efforts to confirm and validate planetary candidates. Candidate identification is supported by both the TESS Science Office systematic vetting process (Guerrero et al. 2021), which produces the official TOI list, and community-driven projects, e.g. Eisner et al. (2021), that contribute additional candidates to the CTOI catalog.

The paper is structured as follows: we begin by detailing the data used for transit signal classification and the modifications to the `ExoMiner++` architecture in Sections 3.4 and 4, including label sources and sector run usage. Section 5 outlines our experimental setup for model learning and evaluation, where we specifically investigate the model’s performance on FFI data compared

to 2-minute data, and assess the impact of supplying neighbor location and brightness information as inputs to the model. The paper concludes in Section 6, which presents the resulting vetting catalog from applying the trained model to FFI TCEs, alongside an analysis of the catalog’s characteristics based on parameters like orbital period and planet radius.

2. RELATED WORK

The development of automated vetting frameworks of transit signals followed the fast increase in the data volume and throughput of exoplanet survey missions in the last decade, with Kepler Mission (Borucki et al. 2010) being a tipping point in that domain. The Kepler Mission provided catalogs of hundreds of thousands of transit signal detections that have made it the most prolific exoplanet survey mission to date, with its data products still actively explored for applications that include, but also go beyond, exoplanet discovery. The ongoing TESS Mission follows in the steps of Kepler and continues to deliver thousands of transit signal events per sector, with more in the years to come. Future missions such as NASA’s Roman Space Telescope (Green et al. 2012) and ESA’s PLAnetary Transits and Oscillations (PLATO; Rauer et al. 2010) pick up such efforts to use transit photometry to unearth new extrasolar planets and fill in the gaps in our understanding of planet population statistics. It is expected that these upcoming missions will create large volumes of data to be added to the already large set being delivered by TESS. Thus, it becomes crucial to develop accurate and efficient automated methods that can sift through these large datasets and uncover planet candidates suitable for follow-up observations. Several transit signal vetters have been developed throughout the last decade, and include if-then rule-based methods (Coughlin et al. 2016; Burke et al. 2020), statistical frameworks (Morton & Johnson 2011; Morton 2012; Morton et al. 2016; Giacalone et al. 2020), and more recently machine learning algorithms such as random forests (Jenkins et al. 2014; McCauliff et al. 2015) and deep neural networks (Shallue & Vanderburg 2018; Ansdel et al. 2018; Armstrong et al. 2020; Valizadegan et al. 2022, 2023).

Regarding the application of transit signal classification frameworks to TESS data, there are a few works that include: (1) `ExoMiner++` (Valizadegan et al. 2025), a multi-branch convolutional neural network (CNN) designed to mimic subject matter experts who examine various false positive tests in the reports produced by the SPOC pipeline DV module. `ExoMiner++` processes several flux time series, periodogram, difference image data, and statistical diagnostics to vet 2-minute cadence TCEs

⁶ <https://archive.stsci.edu/hlsp/tess-spoc/>

from the SPOC pipeline up to the end of Year 5; (2) **AstroNet-Vetting** developed for TESS FFI data (Yu et al. 2019), which is a multi-branch CNN built on the architecture of **AstroNet** (Shallue & Vanderburg 2018) and adds as input a few more diagnostic tests generated by the Quick Look Pipeline (Huang et al. 2020a,b) from calibrated FFI data for early Sectors 1–6; and (3) the work in Tey et al. (2023), another modified version of **AstroNet**, conduct a triaging of QLP FFI TCEs using data from Years 1 through 3, with the main focus of separating periodic eclipsing signals (which include both planets and non-contact eclipsing binaries) from other astrophysical phenomena and instrumental noise.

3. DATA

As a supervised machine learning model, **ExoMiner++** required a dataset of TCEs for training, validation, and evaluation. In this section, we describe the catalogs of TCEs that we use to build our dataset, the sources of data and dispositions for the TCEs, and the preprocessing steps conducted to create a dataset of examples. Throughout this work, a TCE is referred to as TESS SPOC W TCE TIC X - Y - SZ , where X , Y , and Z represent the TIC ID, SPOC planet number, and SPOC sector run associated with the TCE, respectively. W indicates whether the TCE originated from FFI or 2-minute (2-min) data.

3.1. Data Sources

In this work, we use the light curves and other data products generated by the transit searches performed by the SPOC pipeline (Twicken et al. 2020) for both TESS 2-minute and FFI data, which are available at MAST (the latter as HLSP data). Specifically, we use the light curve FITS files to extract the Presearch Data Conditioning Simple Aperture Photometry (PDCSAP; Stumpe et al. 2012, 2014; Smith et al. 2012) flux and the flux-weighted centroid motion time series for each target in any given sector that is associated with a TCE in our dataset, and use the DV XML files to extract the ephemerides, statistics, fit parameters, and difference image data for each TCE.

For our target population, we use TIC-8 (Stassun et al. 2019) as the source catalog for stellar parameters and Gaia DR2 (Gaia Collaboration et al. 2018) as the source for Renormalized Unit Weight Error (RUWE; Lindegren 2018) values.

3.2. Sector Runs

The dataset of TCEs used in this work can be split into two main sets: the SPOC TCEs generated by runs using

2-minute data (from now on referred to as 2-min TCEs), and those generated by the SPOC runs on the FFI data (from now on referred to as FFI TCEs). As with any SPOC DV product, those TCE datasets are available at MAST. The following sector runs were considered for each one of these two populations:

- 2-min TCEs: single-sector runs from Sector 1 through Sector 88, and seventeen multi-sector runs that include Sectors 1–2, 1–6, 1–9, 1–13, 1–36, 1–39, 1–46, 1–65, 1–69, 2–72, 14–19, 14–23, 14–26, 14–41, 14–50, 14–55, 14–60, 14–78, 42–43, and 42–46.
- FFI TCEs: single-sector runs from Sector 36 through Sector 72, and one multi-sector run for Sectors 56–69.

3.3. Label Sources and Assignment

The training and evaluation of our model requires a dataset of labeled TCEs, which entails first finding dispositions based on catalogs of confirmed planets and different types of false positives (e.g., eclipsing binaries, background objects, stellar variability, and instrumental noise); second, matching those events to TCEs through ephemeris matching, following the procedure outlined in (Twicken et al. 2018); and third, mapping those dispositions to a set of labels that are consistent and accurate. It is crucial that we minimize the amount of label noise in our dataset so we can have a high-quality labeled dataset for training and benchmarking our model.

We follow the procedure described in (Valizadegan et al. 2025) and use the Exoplanet Follow-up Observing Program (ExoFOP) TOI catalog⁷, Prsa’s TESS eclipsing binary (EB) catalog (Prša et al. 2022), and TESS-ExoClass (TEC; Burke et al. 2020) tables for SPOC 2-minute and FFI TCEs (for 2-minute TCEs, we use TEC results for all single-sector runs from Sector 1 through Sector 41; for FFI TCEs, we use results from single-sector runs in range 40–73). From the ExoFOP TOI catalog, we use the confirmed planet (CP), known planet (KP), and false positive (FP) dispositioned by the TFOP Working Group (TFOPWG). We consider the KP and CP ExoFOP TOIs that are known brown dwarfs (BDs) based on TFOP Subgroup 1 (SG1) TOI catalog photometric dispositions as false positives and label them as such. TEC flux triage results are used to label TCEs as non-transiting phenomenon (NTP) and Prsa’s TESS EB catalog was used to obtain EB TCEs. At the end of this labeling process, the TCEs that lack a label are labeled as unknown (UNK). To obtain a binary label, TCEs dispositioned as CP and KP are labeled ‘planets’ and those dispositioned as BD, EB (i.e., Prsa’s EBs), FP,

⁷ <https://exofop.ipac.caltech.edu/tess/> downloaded September 22, 2025

and NTP are labeled ‘non-planets’. Refer to [Valizadegan et al. \(2025\)](#) for the details of this labeling procedure.

3.4. Data Preprocessing

The data described in Section 3.1 are preprocessed following the steps in ([Valizadegan et al. 2025](#)) to generate the examples for the TCEs in our datasets. The preprocessing pipeline involves the ephemeris-based (i.e., period, transit duration and epoch of first transit) phase-folding and binning of flux (e.g., primary, secondary, and odd/even events) and flux-weighted centroid motion time series, periodogram computation, and the extraction and preprocessing of in-transit, out-of-transit, and difference flux image data for each TCE. Other scalar features such as the target stellar parameters and TCE fit parameters and statistics computed in the DV module of the SPOC pipeline are used as ancillary features to those higher-dimensionality data. The reader is invited to consult ([Valizadegan et al. 2025, 2022](#); [Twicken et al. 2018](#); [Twicken et al. 2020](#)) for a comprehensive discussion on the data preprocessing and on the SPOC pipeline data products. We made the following changes to the preprocessing pipeline described in ([Valizadegan et al. 2025](#)):

- **Discontinued preprocessing of momentum dump events:** following the conclusions in ([Valizadegan et al. 2025](#)), we chose not to use the momentum dump quality flags as input to our model, as this information was not found to be useful for distinguishing planet TCEs from their non-planet counterparts.
- **Encoding of known neighboring stars’ location and magnitude:** the model described in ([Valizadegan et al. 2025](#)) was provided with information regarding the target location along with the out-of-transit and difference flux images. This set of information enables the model to understand whether there is an offset of the transit source relative to the location of the target (by mapping the target’s TIC coordinates to the CCD pixel frame) and to the out-of-transit centroid. A larger offset might be indicative that the transiting event occurs on a background object. However, the model was not aware of the existence of neighboring stars and their relative magnitudes that show up in the target mask pixels. Without this information, the model is completely blind to scenarios like crowded fields where there can be other stars relatively bright that can be responsible for the transit observed. Thus, we extract information about the location and the magnitude of neighboring stars for each target, and preprocess these information into an image (as an extra input channel in the ‘Difference Image’ branch) and feed it to the

model. Section 3.4.1 describes the preprocessing of the location and magnitude of neighboring stars to create an image that encodes such information.

- **Increased image resolution for difference image data:** [Valizadegan et al. \(2025\)](#) sampled the difference image data using a factor of 3 so the target sub-pixel location could be provided at a higher resolution than pixel-level (e.g., images with an original size of 11×11 px were resampled to a final size of 33×33 px so each pixel in the original image was mapped to a 3×3 px region). Since photocenter offsets of 4–6 arcseconds are generally considered reliable ([Kostov et al. 2025](#)), we adopt a factor of 5 here, which results in image dimensions of 55×55 px. This adjustment provides the model with finer spatial resolution for locating the target and nearby stars.

- **Excluded target image from the ‘Difference Image’ branch:** [Valizadegan et al. \(2025\)](#) used an image to provide the location of the target star to the model. Given that this image only includes the target location information, it is very sparse and difficult for the model to learn from. In this work, instead, we encode the target location by centering the difference image data on the pixel containing the target star. This removes the need to have an extra image channel encoding the target location.

- **Added Signal-to-Noise Ratio (SNR) flux image to ‘Difference Image’ branch:** we computed, pre-processed, and added the SNR flux image as another input channel for the difference image data. The SNR flux image provides information on the significance of the estimated flux difference between out-of-transit and in-transit cadences. It is computed as the difference image flux divided by the uncertainty in each pixel ([Twicken et al. 2018](#)).

3.4.1. Encoding Neighboring Stars’ Location and Magnitude

To encode the location and magnitude of neighboring stars, we queried the TIC-8 catalog to search for stars in a search radius of 168 arcsec (≈ 8 px) around the target’s TIC coordinates. For each target and sector run of interest, we used the World Coordinate System (WCS) stored in the corresponding light curve file to map the celestial coordinates of the neighboring stars into pixel coordinates. Figure 1 shows an example of such search for TIC 83053699 in Sector 57. The two images – difference and out-of-transit fluxes for TCE 1 (TOI 4002.01, a false positive attributed to a nearby eclipsing binary) – show the location of the neighboring stars that were found in a search radius of 168 arcsec, colored as a function of their magnitude value obtained from TIC-8.

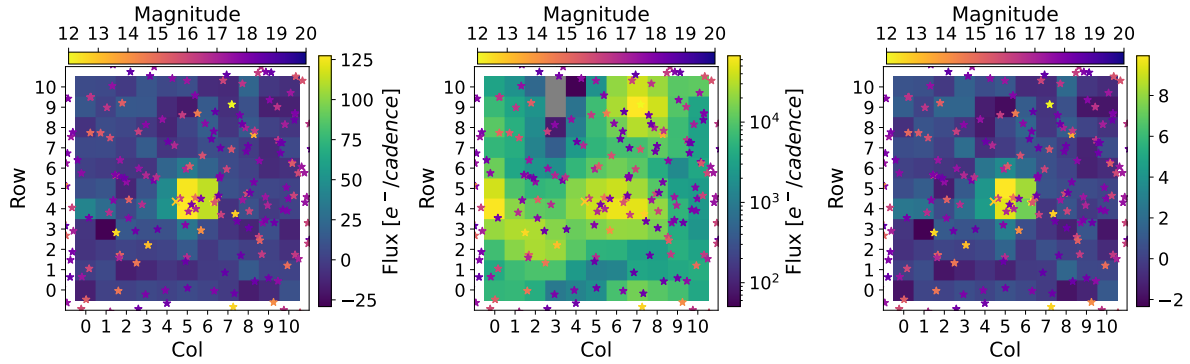


Figure 1. From left to right, the panels display the difference, out-of-transit, and SNR fluxes for TESS SPOC 2-min TCE TIC 83053699-1-S57 (TOI 4002.01). The neighboring stars and target’s TIC-8 coordinates mapped to the CCD frame are identified as stars and as a cross, respectively. Their color encodes the stars’ T_{mag} .

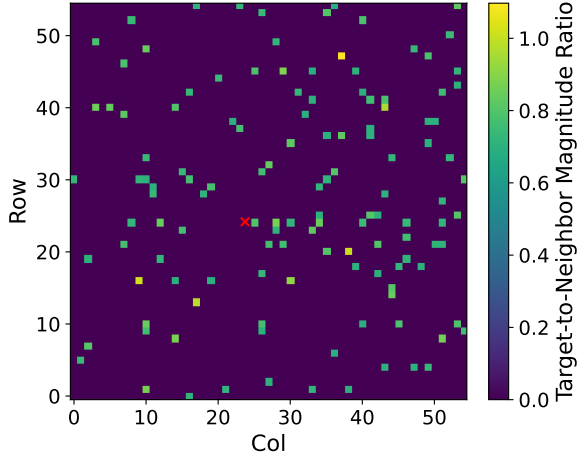


Figure 2. Preprocessed and unnormalized neighboring stars image for TESS SPOC 2-min TCE TIC 83053699-1-S57 (TOI 4002.01). The target’s TIC-8 position is shown as a red cross.

With this catalog of neighboring stars for each target-sector pair (i.e., a target star observed in a given sector), we create the neighbors images for each TCE. We start by excluding multiple different types of neighboring stars:

- Neighbors whose brightness indicates that even a full eclipse could not account for the observed transit depth are excluded. Let T_{mag}^n and T_{mag}^t be the TESS magnitude of a neighboring star and the TESS magnitude of the target, respectively, and let δ be the estimated fractional transit depth of the TCE detected for the target. A neighboring star is excluded if magnitude difference satisfies: $T_{mag}^n > T_{mag}^t - 2.5 * \log_{10}(\delta)$. For neighbors dimmer than this threshold, a complete eclipse would be insufficient to reproduce the measured transit depth in the target light curve.

- All neighboring sources within a pixel are excluded except for the brightest one, when multiple neighbors are present, as the brightest source is the most likely contributor to any off-target transit signal.
- Neighboring stars that fall outside the 11×11 px neighborhood centered on the target pixel are not included. While it is possible that the stars outside of this region are the transit source, encoding their location accurately within the image representation is nontrivial. One potential alternative to include information about stars outside of the patch that still bleed light towards the target neighborhood, would be to extend the edges of the image by 1 px to encode neighbors outside of the 11×11 px neighborhood, however that also comes with drawbacks in terms of distorting the distance of such neighbors to the target star, and requiring the difference image data to be extended in a similar way. To avoid these challenges, and because it is unlikely that neighbors in this situation are the transit source, we exclude them when creating the neighbors image.

After excluding those neighboring stars, we set the value of a pixel to the ratio of the target’s magnitude to the neighbors’ magnitude if there is a neighboring star; otherwise, it is set to zero. With this encoding, pixels with values greater than one represent neighbors that are brighter than the target star, while those with value less than one are dimmer. Figure 2 shows the neighbors’ image for the same TCE in Figure 1 after preprocessing the neighbors data by following these steps. Contrary to the normalization performed for the difference, out-of-transit, and SNR flux images, where we standardize the images using statistics computed from the training set, for the neighbors images we conduct fixed min-max normalization. This choice was motivated by the fact that many pixels have no neighboring stars, resulting in ratio values of zero and consequently an extremely small

Table 1. TESS 2-min SPOC TCE and Event Counts.

	Classes	Exoplanets		Non-planets			
	Subclasses	KP	CP	BD	EB	FP	NTP
TCE Counts	Count (Percentage)	2,587 (4.40%)	2,852 (4.85%)	68 (0.12%)	11,794 (20.07%)	2,713 (4.62%)	38,747 (65.94%)
	Total (Percentage)	5,439 (9.26%)		53,322 (90.74%)			
Event Counts	Count (Percentage)	546 (13.51%)	546 (13.51%)	19 (0.47%)	2,292 (56.72%)	638 (15.79%)	N/A (-%)
	Total (Percentage)	1,092 (27.02%)		2,949 (72.98%)			

Table 2. TESS FFI SPOC TCE and Event Counts.

	Classes	Exoplanets		Non-planets			
	Subclasses	KP	CP	BD	EB	FP	NTP
TCE Counts	Count (Percentage)	806 (1.14%)	1,000 (1.42%)	30 (0.04%)	4,607 (6.54%)	1,208 (1.71%)	62,787 (89.14%)
	Total (Percentage)	1,806 (2.56%)		68,632 (97.44%)			
Event Counts	Count (Percentage)	364 (14.46%)	370 (14.70%)	14 (0.56%)	1,332 (52.92%)	437 (17.36%)	N/A (-%)
	Total (Percentage)	734 (29.16%)		1,783 (70.84%)			

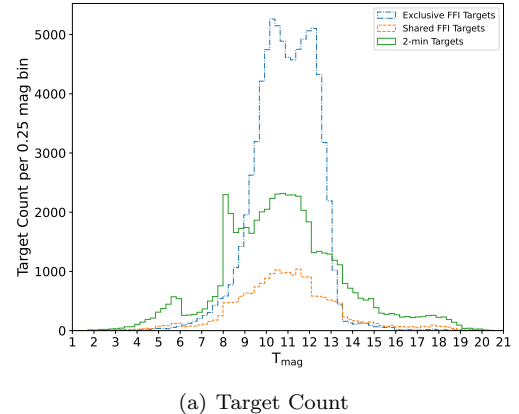
standard deviation of pixel values, which is required for standardization. Such small standard deviation can cause the non-zero values to become disproportionately large, potentially disrupting model training, hindering convergence, and impairing overall learning. The target-to-neighbor magnitude ratio of all targets in our dataset is not larger than 5, meaning that any neighbor’s magnitude is not more than five magnitudes larger than the target star. Because of that, we use a factor of 5 to normalize these ratios, ensuring that they are in $[0, 1]$.

3.5. Dataset

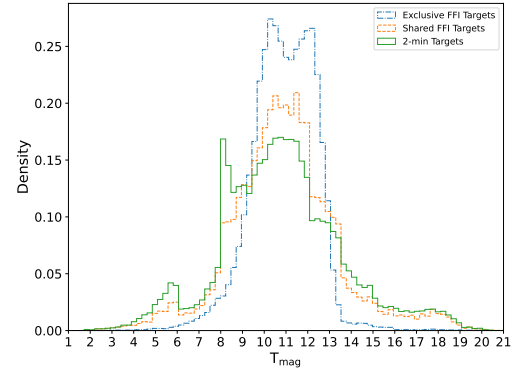
Preprocessing the 2-minute and FFI data (i.e., light curves and DV SPOC XML files) resulted in datasets of 268,787 and 222,054 TCEs, respectively. For the FFI data, 70,438 TCEs ($\approx 31.72\%$) are labeled using the procedure discussed in Section 3.3, leaving 151,616 as UNK TCEs.

Tables 1 and 2 show the distribution of TCEs and events in the 2-minute and FFI labeled datasets as a function of their binary label (i.e., planet or non-planet class) and disposition (i.e., subclass). Given that more than one TCE can be associated with the same event (e.g., TOI) due to the observation behavior of TESS, these tables also break down the dataset in terms of these unique transiting objects. NTPs are not federated to any transit event given that they are not associated with real astrophysical transiting phenomena. For that reason, we have excluded these TCEs from the event count.

As indicated by the numbers reported in these two tables, the 2-minute dataset contains a larger number of TCEs confirmed as ExoFOP TOIs than the FFI dataset. This difference is primarily due to the more extensive sector coverage, particularly the multi-sector observations, available for the 2-minute data, which increases the likelihood of detecting longer-period TOIs and plan-



(a) Target Count



(b) Target Density

Figure 3. Target population for the 2-min and FFI TCE datasets as a function of T_{mag} .

ets with smaller radii, and to the smaller number of sectors with HLSP SPOC FFI data products available at this moment.

Figure 3 shows the distribution of targets in the 2-min and FFI TCE datasets (including unlabeled TCEs) as a function of T_{mag} . The two distributions have a significant

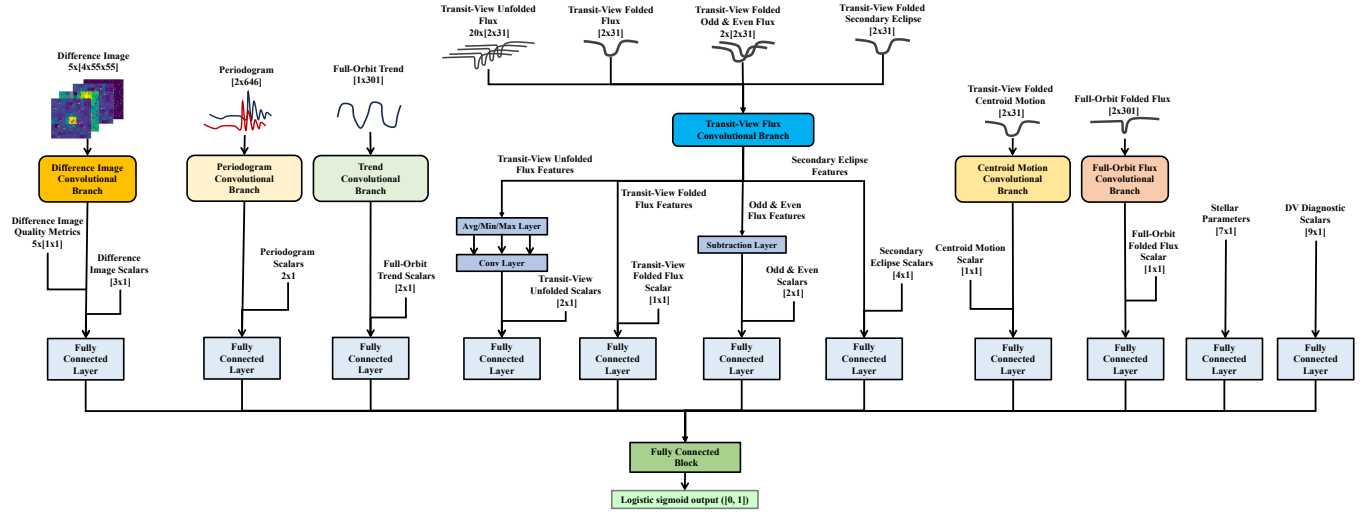


Figure 4. High-level depiction of the new `ExoMiner` architecture used in this work. The details of this model are described in Section 4.

overlap, although the FFI target population exhibits a higher concentration of targets around $T_{mag} = [9, 13]$, and the 2-minute target population distribution shows a slightly heavier tail for both brighter and dimmer targets. These distinct distributions reflect the differing selection criteria for 2-min and SPOC FFI targets, highlighting the potential for discovering new planetary candidates within the remaining unvetted TCEs.

4. MODEL

The model used in this work, hereafter referred to as `ExoMiner++ 2.0`, builds on `ExoMiner++` (Valizadegan et al. 2025). A high-level depiction of this architecture is shown in Figure 4, and a detailed version that includes the dimension of the feature maps after each layer can be found on Zenodo (Martinho & Valizadegan 2025). Several architectural modifications involve changes to the branches responsible for processing specific inputs, as described below:

- **Merged ‘Unfolded Flux’ branch with the other transit-view flux branches:** given that the unfolded binned flux time series shares similarities with the phase-folded and binned flux time series (i.e., they are all transit views of the primary or secondary transits of the TCE), we decided to add the 20 sampled phases of the unfolded flux time series (including the variability time series as the second channel) to the existing four views (primary, secondary, and odd-even) to be processed by the same convolutional branch. The extracted features from the unfolded time series input are then processed separately using the same method described in Valizadegan et al. (2025).
- **Moved transit source offset estimate and uncertainty to ‘Difference Image’ branch:** the transit

source computed by the DV module of the SPOC pipeline is estimated from the difference image data. To take that into account, we moved this scalar feature (along with its uncertainty) from the ‘Centroid Motion’ branch to the ‘Difference Image’ branch.

The remaining changes are related to improvements on the extraction and processing of features through the CNN model and include:

- **Adding global average pooling layers:** we added global average pooling layer instead of basic flattening layer in the end of each convolutional branch. This decreases the number of features at the end of the convolutional branch to the number of channels set for the final convolutional layer, thus leading to a smaller model that is less prone to overfitting. This type of layer has been used in many state-of-the-art (SOTA) CNN architectures such as ResNet (He et al. 2016) and Inception (Szegedy et al. 2015), especially those designed for classification tasks.
- **Replacing max pooling with strided convolution:** We replaced the max-pooling layer at the end of each convolutional block with a strided convolutional layer applied at the block input (i.e., the first convolutional layer uses a stride greater than one and no padding, resulting in a reduction of the feature-map resolution). A strided convolution performs downsampling by sliding the filter over the input feature maps with a step size larger than one, thereby reducing the spatial dimensions of the output. This modification is inspired by state-of-the-art architectures, such as more recent variants of ResNet (He et al. 2016) and YOLOv5 (Redmon et al. 2016), which replace pooling operations with strided convolutions. By adopting strided convolutions, the model is able to learn task-

specific downsampling operations, rather than relying on a fixed transformation such as max pooling.

- **Preserving spatial resolution for difference images:** since detecting small transit source offsets is critical, we did not apply downsampling approaches like strided convolution and max pooling to the ‘Difference Image’ branch. Downsampling can discard fine-grained positional information which are needed to detect subtle offsets.
- **Adding batch normalization and skip connections:** to improve the stability and convergence of the models during training, a batch normalization layer (Ioffe & Szegedy 2015) was introduced after each convolutional layer. Additionally, a residual block (He et al. 2016) was added to the output of each convolutional block to provide better gradient flow and allow feature reuse.
- **Adding layer normalization:** to balance the contribution from all branches in the model, we applied a layer normalization layer (Ba et al. 2016) after concatenating the features extracted from all branches. These layers stabilize training by normalizing the activations across features. Fully connected (FC) layers are able to learn and adjust the weights to compensate for scale differences in the features; however, by applying these layers, we reduce the risk of one branch’s features overshadowing the others due to their raw magnitude, since features with larger magnitudes produce larger gradients that can dominate the updates during training. To further improve stability during training and reduce overfitting, we added one normalization layer after each FC layer in the large classification head.

5. EXPERIMENTS

In this section, we start by describing the setup used for running the experiments in this work. Specifically, we outline the data splits used for training and testing, the model training process, and the set of evaluation metrics used. We then detail the primary experiments conducted in this work, which include using both 2-minute and FFI data to train the models. The `ExoMiner` code is publicly available on GitHub⁸, and the preprocessed datasets of TESS SPOC 2-minute and FFI TCEs used in this work are available on Zenodo (Martinho & Valizadegan 2025).

5.1. Experimental Setup

To evaluate the model under different data splits, we conducted 5-fold cross-validation (CV) experiments, providing a more reliable estimate of performance across

multiple splits. This approach ensures that all available data are used for both training and evaluation and helps assess generalization more robustly. The data are split into five folds such that the TCEs associated with the same target are included in the same fold. Given that all TCEs generated from the same target light curve and pixel data are either part of the training or test sets in any given CV iteration, we minimize data leakage. Furthermore, to ensure that the folds have approximately the same distribution of planets and non-planets as the overall dataset, we use a greedy strategy to assign TCEs to cross-validation folds. For each target, all its TCEs are grouped together and assigned to the fold that holds the fewest planet TCEs. This iterative process ensures that the distribution of planet across folds remains as balanced as possible.

Model performance is evaluated by using the following metrics: area under the precision-recall (PR AUC) and the receiver operating characteristic curves (ROC AUC), as well as precision, recall and accuracy at a classification threshold of 0.5. Given that this work emphasizes the vetting of TCEs (in contrast to planet validation) and we aim to assess performance under stringent decision thresholds, we additionally report recall at the operating point where precision is 95%, and precision at the operating point where recall is 95%. The first metric indicates how many true planet TCEs are correctly identified when we require very few false positives (high precision), while the second shows how many predictions are correct when we aim to capture nearly all true planets (high recall). Together, these metrics illustrate the trade-off between completeness and reliability under strict classification criteria.

To evaluate and compare the two models, we report a descriptive performance per model, and an inferential, paired comparison based on bootstrapping aggregated out-of-fold predictions. For descriptive reporting, we compute for each model the mean and standard deviation (SD) of the metrics across the five held-out test folds from cross-validation. This provides a sense of the model’s stability across different partitions of the data. However, these fold-level estimates are not independent because training sets overlap, which induces correlation among folds. As a result, naive significance tests on these five numbers can underestimate variance and inflate Type-I error rates (Dietterich 1998; Nadeau & Bengio 1999). Thus, mean \pm SD across folds should be interpreted as a descriptive measure of variability, and not as a formal test of superiority.

To formally assess whether one model outperforms the other, we use a paired, stratified, instance-level bootstrap on the combined out-of-fold predictions from all five

⁸ <https://github.com/nasa/ExoMiner>

Table 3. Binary classification performance of **ExoMiner** models for the test sets of the 5-fold cross-validation experiment using multi-source data from both 2-min and FFI sources. Precision, recall, and accuracy are computed at a classification threshold of 0.5. Mean and standard deviation estimates are computed across the CV iterations. The best performer is highlighted in bold. Differences are not claimed to be statistically significant unless stated otherwise.

Model	Precision & Recall	PR AUC	ROC AUC	Accuracy	Precision @ 95% Recall	Recall @ 95% Precision
ExoMiner++	0.913 ± 0.027 & 0.912 ± 0.026	0.962 ± 0.012	0.996 ± 0.002	0.990 ± 0.002	0.872 ± 0.015	0.798 ± 0.113
ExoMiner++ 2.0	0.922 ± 0.019 & 0.865 ± 0.019	0.958 ± 0.006	0.995 ± 0.002	0.988 ± 0.002	0.832 ± 0.026	0.751 ± 0.074

Table 4. Subclasses recall at classification threshold of 0.5 for the test sets of the 5-fold cross-validation experiment using multi-source data from both 2-min and FFI sources. Mean and standard deviation estimates are computed across the CV iterations. The best performer is highlighted in bold. Differences are not claimed to be statistically significant unless stated otherwise.

Model \ Recall	KP	CP	BD ^a	EB	FP	NTP
ExoMiner++	0.915 ± 0.022	0.906 ± 0.045	0.686 ± 0.188	0.997 ± 0.002	0.876 ± 0.068	$0.999 \pm 5e-4$
ExoMiner++ 2.0	0.876 ± 0.046	0.852 ± 0.030	0.876 ± 0.100	0.996 ± 0.004	0.903 ± 0.040	$0.999 \pm 1e-4$

^aBD subclass has only 98 examples; therefore, recall values may not be statistically significant beyond two decimal places.

test sets. This approach resamples instances with class-stratification and computes the difference in each metric ($\Delta = metric_{ModelB} - metric_{ModelA}$) for each bootstrap replicate. From these replicates, we derive percentile confidence intervals (CIs) for the difference and assess both statistical significance (i.e., whether the CI excludes zero) and practical significance (i.e., whether CI clears a pre-specified effect size threshold ϵ). This method leverages all available out-of-fold predictions rather than reducing the comparison to five fold-level aggregates, leading to substantially greater statistical efficiency in large-sample settings relative to fold-level tests. It avoids parametric assumptions about the distribution of fold means and exploits the paired nature of per-instance predictions, while conditioning on the fitted models obtained from the CV experiments (Efron & Tibshirani 1994).

We computed 5,000 stratified bootstrap replicates, and estimated the 95% confidence intervals for each metric (i.e., significance level set to $\alpha = 0.05$). The effect size thresholds were chosen to reflect operational impact (e.g., 1% increase in performance). For all proportion-based metrics (i.e., recall, precision, and accuracy) and PR AUC, the effect size threshold was set to $\epsilon = 0.01$, which means that a 1% difference is considered practically significant. As for ROC AUC, the threshold was set to $\epsilon = 0.005$ since it is less sensitive to class imbalance.

For each cross-validation iteration, we train a set of 10 models and construct an ensemble by averaging their prediction scores using the mean. This approach helps reduce variability caused by random weight initialization

and the inherent stochasticity of mini-batch gradient descent during optimization. By training multiple models with different weight initializations, the ensemble captures variations in local minima encountered during the optimization of the loss function, resulting in a more accurate estimate of the model’s performance.

All models are trained for 300 epochs, optimized using binary cross-entropy as the loss function and the Adam optimizer (Kingma 2014) ($\beta_1 = 0.900$, $\beta_2 = 0.999$, $\epsilon = 1e-8$). Model selection is performed using early stopping with a patience of 20 epochs to prevent overfitting; i.e., if no improvement in the validation PR AUC is observed after 20 epochs, the training is stopped, and the model instance at that point is selected as the final model. The CV dataset can be found on Zenodo (Martinho & Valizadegan 2025).

5.2. Multi-source Learning

As the ongoing SPOC planet searches produce results for more sector runs, the number of FFI TCEs is expected to grow and surpass the 2-minute results. However, the current number of sector runs performed for the FFI data is significantly smaller than those for the 2-minute data, and only a single multi-sector run has been conducted as mentioned in Section 3.2. For this reason, using the 2-minute labeled dataset for training the model might result in improved performance on FFI data. Following the work in Valizadegan et al. (2025), we conducted multi-

source learning (Zhuang et al. 2020) using as sources the TESS SPOC 2-min and FFI TCEs datasets for training.

The FFI and 2-min datasets differ in a few key important ways: 1) Cadence: the 2-minute data have a shorter cadence, whereas TESS full-frame images are sampled at either 30 min, 10 min, or 200 s depending on the sector. The SPOC pipeline resamples the light curves to a common cadence of 10 minutes for the multi-sector runs since the S14–S55 search, partially reducing the difference; 2) Systematics correction: the 2-minute light curves benefit from more effective systematics correction, including less blending and crowding on average; 3) Vetting quality: the 2-minute data have higher-quality dispositions due to more extensive and focused vetting of transit signals. Although the 2-min targets also appear in FFI data, the shorter and fewer sector runs for these data limit the detection of TCEs by the SPOC pipeline, particularly for longer-period TOIs. Additionally, targets observed exclusively in FFI data have received less scrutiny to date; and 4) Target population: FFI data cover a more diverse target population, including those targets already observed for 2-minute data as well as many more fainter targets.

Multi-source learning allows the model to simultaneously learn shared representations in a larger combined dataset that generalizes across both domains (i.e., the two collection modes), which can be more effective than fine-tuning (e.g., pre-training on the 2-min dataset and then continuing training on the FFI dataset) since that may overwrite useful features learned from the 2-min data. In this setting, the model is exposed during training to different noise levels and target populations which provides better generalization to new, unseen sectors.

5.3. Results and Discussion

In this section, we start by presenting the results of the 5-fold CV experiments using **ExoMiner++** as the baseline study. Both **ExoMiner++** and **ExoMiner++ 2.0** are evaluated on the same multi-source 5-fold CV dataset. We also investigate the change in performance between the two data sources.

5.3.1. Cross-Validation Results

Table 3 presents the overall performance of the **ExoMiner++** and **ExoMiner++ 2.0** models across a multi-source 5-fold cross-validation procedure, evaluated using standard binary classification metrics. The first thing to notice is that the results for **ExoMiner++** are in line with those reported in Valizadegan et al. (2025) when the model is trained on TESS 2-min data. Even though the dataset used in the current work has a different data distribution and includes more sector runs and FFI TCEs, the overall performance metrics remain consistent.

ExoMiner++ and **ExoMiner++ 2.0** show small standard deviations, suggesting stable performance across folds. **ExoMiner++** shows higher standard deviation for recall at 95% precision, indicating some operating-point sensitivity under fold changes. At this operating point, **ExoMiner++** achieves a recall of approximately 80%, meaning that 95 out of 100 predicted planets are true exoplanets, and 80 out of 100 exoplanets are retrieved. As an example, if we assume a catalog of 1,000 objects following the same ratio of planet TCEs to non-planet TCEs as our combined 2-min/FFI dataset (approximately 5.6% planet TCEs vs. 94.4% non-planet TCEs), then at an operating point of 95% precision and 80% recall, the model would predict 47 TCEs as planets, of which 2 are non-planets. Furthermore, the model would miss 11 planet TCEs out of the 56 present in the catalog.

Table 4 details the recall values for each subclass at a fixed classification threshold of 0.5, highlighting the models' ability to correctly identify positive instances within each specific subclass. Across the five folds, these results combined with the ones shown in Table 3 suggest that **ExoMiner++** has higher recall, accuracy, PR AUC, and ROC AUC, whereas **ExoMiner++ 2.0** shows stronger performance on specific negative subclasses (FP, BD). Overall, **ExoMiner++** offers stronger global performance and recall, whereas **ExoMiner++ 2.0** provides targeted improvements in specific negative subclasses.

Since we aim to assess whether incorporating neighbors' data improves the model's ability to reduce confidence for TCEs with observable transit-source offsets near bright stars, we also examined the recall of both models for nearby false positives, specifically TOIs classified as nearby planet candidates and eclipsing binaries in SG1. The recall for these nearby FPs is 0.92 and 0.94 for **ExoMiner++** and **ExoMiner++ 2.0**, respectively. Figure 5 shows the distribution of scores for the two models for both planet and nearby FP TCEs. The shift in both distributions indicates that **ExoMiner++ 2.0** lowered the scores of all objects, true planets or background transits. As such, it is more conservative.

A similar behavior is also observed when we plot the mean average score for planets and nearby FPs as a function of the CROWDSAP metric (Figure 6). TCEs observed in multiple sectors were excluded from this analysis because, in those cases, there are multiple CROWDSAP metrics available, one for each sector where the target was observed, and there is no straightforward method to aggregate these metric values into a single statistic. The CROWDSAP metric in TESS data quantifies the fraction of flux in the photometric aperture that originates from the target star; values near unity indicate minimal contamination, whereas lower values

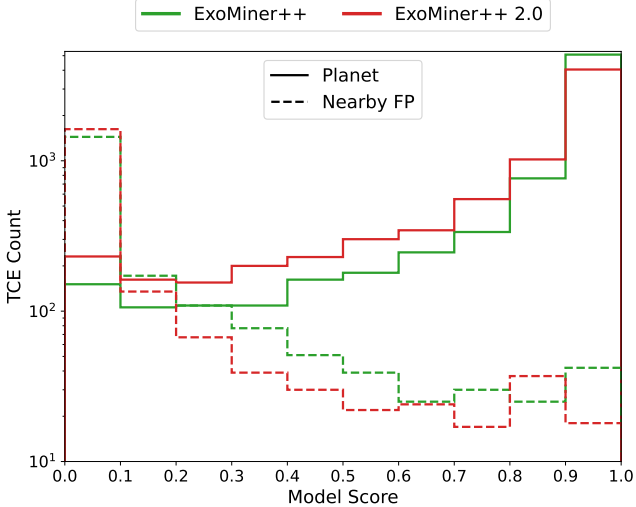


Figure 5. Distribution of ExoMiner++ and ExoMiner++ 2.0 scores for planet and nearby false positive TCEs.

indicate significant flux contribution from nearby stars or background sources. As the contamination increases (i.e., lower CROWDSAP values), both models exhibit a decrease in the planet average score, while the average score for nearby FPs remains consistent (results below CROWDSAP ≈ 0.5 are less reliable given that those bins contain fewer than 100 TCEs). However, even in cases where nearly all of the flux in the aperture comes from the target star (i.e., CROWDSAP close to 1), ExoMiner++ 2.0 still shows an average lower score for both planet and nearby FP TCEs. This conservativeness translates into a tradeoff, as the model degrades its performance on planet TCEs to correctly classify nearby false positives. Three hypotheses can explain this: 1) the large pixel scale (21 arcsec) means that even in moderately crowded fields, the light from the target star is often mixed with nearby stars that fall into the same photometric aperture or even the same pixel and can still lead to errors in the transit source location estimation even when conducting difference image analysis. This limitation constitutes a lower bound that ultimately limits the capability of the model to separate on-target transits from background sources; 2) the small number of nearby FPs relative to the size of the dataset, combined with the joint optimization of the model means that it is challenging for the model to optimize its ‘Difference Image’ branch to learn features useful for detecting real transit source offsets. For example, pretraining the difference image branch on a dedicated task that distinguishes on-target transit signals from those originating in nearby stars could enable the branch to learn discriminative representations for this scenario; 3) no dedicated hyperparameter optimization (HPO) was performed for this architecture, particularly

the ‘Difference Image’ branch. We expect that by conducting a new HPO run we can find a more optimal architecture that can use the difference image data more effectively, including the neighbors information. Other potential future improvements to enhance the performance of the difference image branch in cases where the transit source may be a neighboring star include incorporating a lightweight spatial attention mechanism inspired by (Woo et al. 2018) to guide the model toward salient regions of the image such as the transit signal location, while suppressing irrelevant areas like pixels without known stars. Another promising direction is to select difference images from sectors with higher quality metrics rather than relying on random sampling with replacement, ensuring the model is exposed to a set of higher-quality inputs.

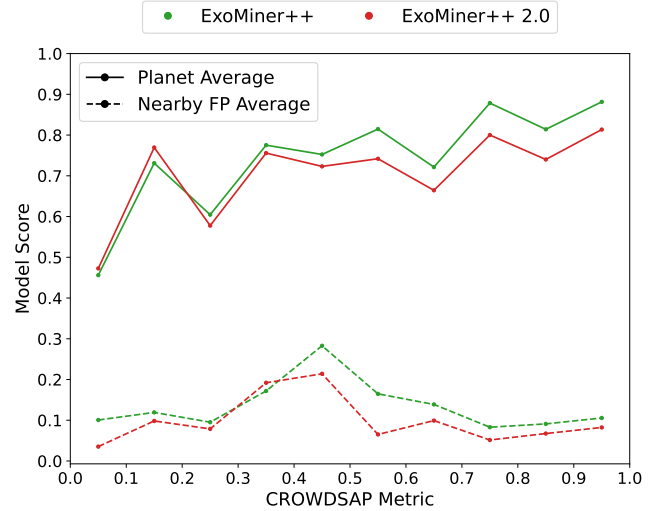


Figure 6. Average ExoMiner++ and ExoMiner++ 2.0 score for planet and nearby false positive TCEs as a function of CROWDSAP metric.

5.3.2. Comparison Between Data Sources

As outlined in Section 5.2, the 2-min and FFI datasets exhibit distinct observational and noise characteristics, which can influence model behavior. In this section, we start by comparing the overall performance on these two datasets. To remove confounding effects from this analysis, we exclude NTP TCEs since this subset is dependent on the availability of TEC’s flux triage results. As mentioned in Section 3.3, we had access to an inconsistent set of these results: for 2-min data we used the flux triage results for single-sector runs S1 through S41, while for FFI we had results for single-sector runs S40 through S73. Besides not having the results for the same sector runs, the numbers of NTP TCEs generated by

Table 5. Comparison between 2-min and FFI datasets. NTP TCEs were excluded and only TCEs from the same sector runs were considered from both datasets.

Category	2-min	FFI
TCEs	6,020	6,419
Targets	2,060	2,226
Events	2,096	2,241
KP TCEs (%)	801 (13.31%)	604 (9.41%)
CP TCEs (%)	669 (11.11%)	776 (12.09%)
BD TCEs (%)	13 (0.22%)	16 (0.25%)
EB TCEs (%)	3,747 (62.24%)	4,051 (63.11%)
FP TCEs (%)	790 (13.12%)	972 (15.14%)

these two results varies significantly as shown in Tables 1 and 2. Furthermore, the SPOC planet searches for FFI data start only with Sector 36, and so far only one multi-sector run was conducted. Because of this, the number of multi-sector runs from 2-min data is significantly larger, and on average longer than the single multi-sector run conducted for FFI data (S56–S69). With this bias in mind, for this analysis we considered only TCEs from the planet searches that use the same sectors, which in this case are all single-sector runs from Sector 36 through Sector 72, totaling 37 runs. Given that the ephemeris matching was conducted for the same sector runs and using the same label sources, the only differences in these two sets come from the target selection criteria for FFI and 2-min data, and the operation of the SPOC pipeline when performing planet searches in these two data collection modes. Table 5 shows the number of TCEs, targets, and events (i.e., TOIs and Prsa’s EBs) for 2-min and FFI data after applying these filters.

As expected, the FFI data contain more TCEs as the number of targets selected for FFI planet searches was larger than for 2-min. Following this trend, the number of events matched to TCEs was also larger. However, both datasets have targets and events that are exclusive to each other. In the case of events, the number of these objects that are shared between 2-min and FFI datasets is 1,708, while 533 and 388 are found exclusively in FFI and 2-min data, respectively. Interestingly, the number of detected KP TCEs in 2-min data is significantly larger than for FFI data, while a similar trend is shown for CP TCEs but favoring FFI data. Besides those differences, the FFI dataset also shows significantly more FP TCEs detected than the 2-min counterpart.

Table 6 shows the performance metrics for `ExoMiner++ 2.0` on these two datasets. The metrics were computed by aggregating the test set predictions across all CV iterations. Overall, the 2-min dataset shows higher per-

formance, including on normalized PR AUC and ROC AUC, both of which are considered less sensitive to variations in class distribution across the two datasets. The normalized PR AUC is computed as:

$$\text{Normalized PR AUC} = \frac{\text{PR AUC} - \gamma}{1 - \gamma}, \quad (1)$$

$$\gamma = \frac{N_{\text{pos}}}{N_{\text{total}}}, \quad (2)$$

where γ denotes the prevalence of positive examples in the dataset.

To investigate the causes behind the lower performance in the FFI dataset, we examined parameters that could explain these differences. More concretely, we analyzed the distribution of targets as function of T_{mag} and Gaia RUWE, as well as the distribution of TCEs as function of their multiple event statistic (MES) and TCE model SNR. None of these parameters showed a clear shift in distribution between the two datasets. However, the distribution of the CROWDSAP metric revealed a noticeable shift for FFI targets toward lower values (Figure 7). A substantial fraction of FFI targets exhibit CROWDSAP values below 0.9, meaning that at least 10% of the flux in the aperture originates from other sources. Such contamination can dilute transit depths, bias planet radius estimates, reduce MES and SNR, and introduce systematics that are more difficult to correct by algorithms such as the PDC module in the SPOC pipeline. Furthermore, blended eclipsing binaries and variable stars within the aperture can mimic transit-like signals, increasing the false positive rate. Although MES and SNR distributions do not appear strongly affected, the deterioration in `ExoMiner++ 2.0` performance suggests that contamination impacts other classification-relevant features, such as transit shape and detrending quality.

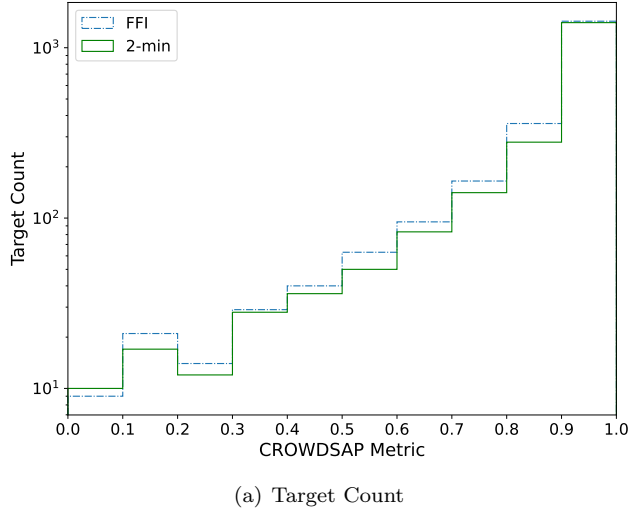
6. VETTING FFI TCEs

To vet unlabeled FFI TCEs, we employed the ensemble of trained models from the `ExoMiner++ 2.0` CV experiment. Although training a single final model using the same setup would simplify deployment, it would likely be less robust than an ensemble trained on different subsets of the data. Leveraging the CV ensemble improves robustness and reduces variance in predictions for the unlabeled dataset. For each TCE, we aggregate predictions from the five CV folds to compute the mean and standard deviation, providing both a ranking metric and an uncertainty estimate. The mean prediction can be used to prioritize candidates, while the standard deviation reflects model disagreement. High uncertainty indicates

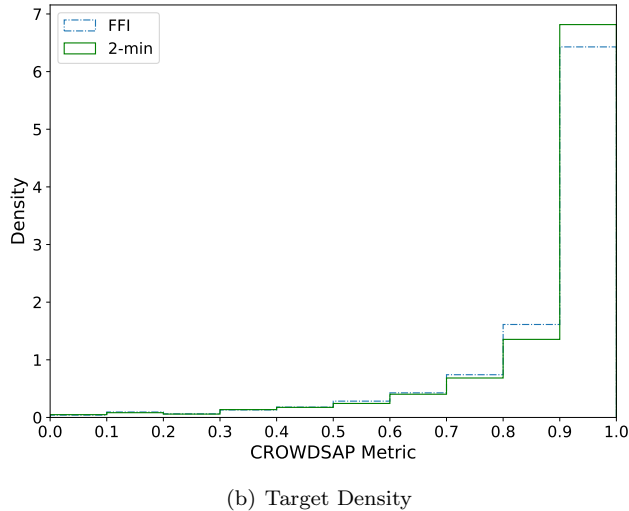
Table 6. Binary classification performance for **ExoMiner++ 2.0** from CV experiment computed separately for the 2-min and FFI datasets. Precision, recall, and accuracy are computed at a classification threshold of 0.5. The best performer is highlighted in bold. Point estimates are computed across the CV iterations by aggregating all test sets.

Source	Precision & Recall	PR AUC ^a	Normalized PR AUC	ROC AUC	Accuracy ^a	Precision @ 95% Recall ^a	Recall @ 95% Precision ^a
2-min	0.937 & 0.845	0.967	0.957	0.989	0.948	0.876	0.767
FFI	0.917 & 0.854	0.952	0.938	0.987	0.952	0.854	0.651

^aThese metrics should be compared with caution because they are sensitive to class distribution differences between datasets.



(a) Target Count



(b) Target Density

Figure 7. Target population for the 2-min and FFI TCE datasets as a function of CROWDSAP Metric.

ambiguous signals, which may correspond to borderline cases and unusual morphologies, and thus making them scientifically interesting.

The complete table of predictions for UNK TCEs is available on Zenodo (Martinho & Valizadegan 2025). Table 7 describes the contents of this table, which lists unlabeled TCEs ranked by decreasing prediction score. In addition to TCEs corresponding to TOIs with labels

Table 7. Scores and dispositions of **ExoMiner++ 2.0** model for unlabeled FFI SPOC TCEs. This table describes the available columns. The full table is available online.

Column	Description
uid	Unique TCE ID that includes TIC ID, planet number, and sector run in the format tic_id-s poc_tce_planet_number-Sector_run
target_id	TIC ID
tce_plnt_num	SPOC TCE planet number
sector_run	SPOC sector run
tce_period	TCE period (days)
tce_duration	TCE duration (hours)
tce_time0bt	TCE epoch (BTJD)
tce_depth	TCE depth (ppm)
tce_prad	TCE planet radius (Earth radii)
mes	TCE MES
tce_model_snr	TCE model SNR
tmag	TESS magnitude
ruwe	Gaia DR2 RUWE
n_tois_in_tic	Number of known TOIs in the TIC ^a
tois_in_tic	List of known TOIs in the TIC ^a
DV full report	URL to the DV full report in MAST
DV summary report	URL to the DV summary report in MAST
DV mini report	URL to the DV mini report in MAST
score_cv_iter_i	For $i \in [0, 5]$, score of the ExoMiner++ 2.0 model trained on CV fold i
mean_score	Average score of 5 ExoMiner++ 2.0 models
std_score	Standard deviation of the scores of 5 ExoMiner++ 2.0 models
model_label	'PC' if ExoMiner++ 2.0 score > 0.5 , 'FP' otherwise

^a As of September 22, 2025.

we treat as uncertain (e.g., PC), the table also contains some TCEs associated with TOIs that we treat as certain (e.g., KP). These cases arise for several reasons: (1) failure to match a TCE to its corresponding TOI due to uncertainties in the estimated ephemerides and the propagation of errors. The matching procedure relies on period and epoch estimates, and significant uncertainties, particularly when epochs are widely separated, can

prevent proper alignment of transit events. This issue is more common for single-sector and longer-period TCEs, where fewer observed transits lead to poorer ephemeris constraints; (2) failure to match a TCE to a TOI because the period detected by the SPOC pipeline is a multiple or fraction of the object’s true period; and (3) promotion of objects to TOIs after the ExoFOP TOI catalog used in this work was downloaded.

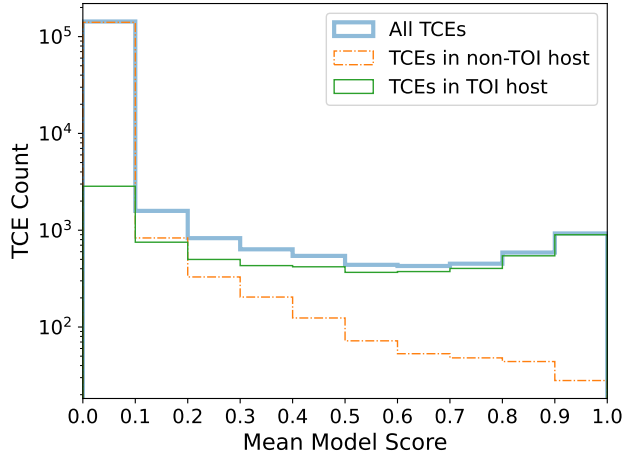


Figure 8. Distribution of ExoMiner++ 2.0 mean scores for unlabeled FFI SPOC TCEs.

The predicted mean score distribution for the unlabeled FFI TCEs is presented in Figure 8, which also distinguishes between candidates orbiting targets with known TOIs and those orbiting stars with no known TOIs. Because they are less likely to be previously cataloged, the set of TCEs associated with targets without known TOIs is considered a higher priority for further vetting. To quantify the TCEs in the full set of unlabeled examples, we find that 2,831 TCEs score above 0.5, 926 above 0.9, and 447 above 0.95, while none scored above 0.99.

Figure 9 shows the distribution of the orbital period against planet radius for TCEs whose scores were above 0.5. As expected, most TCEs have an orbital period shorter than the duration of a single sector. This occurs because the FFI dataset currently lacks multi-sector runs and yields on-average lower SNR for longer-period TCEs due to the fewer observations available which in turn lowers the model’s predicted scores for those examples. The longest-period TCE (≈ 106 days) has a mean score of about 0.59 and an estimated planet radius of approximately $11.5 R_{\oplus}$. A cluster of TCEs with scores greater than 0.9 is visible for orbital periods in the range of $[2, 5]$ days and planet radius in the range of $[10, 20] R_{\oplus}$, consistent with the expected parameters for hot Jupiters.

For the 58 TCEs in the range of potential terrestrial planets ($R_{\oplus} < 1.7$), there is no clear pattern in their distribution of period and planet radius.

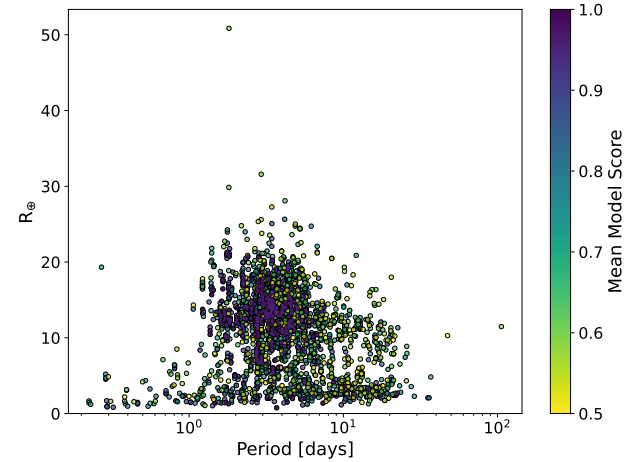


Figure 9. Distribution of SPOC DV estimated orbital period versus planet radius for UNK FFI TCEs with ExoMiner++ 2.0 mean scores greater than 0.5. Each data point represents a TCE and is colored based on the assigned prediction score.

7. CONCLUSIONS

In this work, we extended the ExoMiner++ framework to vet TCEs detected in TESS FFI data. By adapting the original architecture and preprocessing pipeline to account for the unique characteristics of FFI observations (such as longer cadence and increased flux contamination), we demonstrated that deep learning models can generalize effectively beyond the 2-minute cadence domain. Key improvements included the integration of neighboring star information, higher-resolution difference images, and additional image channels such as difference image SNR, which collectively enhanced the model’s ability to identify off-target transit sources. Our experiments using multi-source learning across both 2-minute and FFI datasets showed that leveraging the larger and better-labeled 2-minute dataset improves performance on FFI data, mitigating the limitations imposed by fewer multi-sector runs and noisier light curves. The new architecture achieved reasonable precision and recall under stringent operating points, enabling reliable discrimination between planets and false positives. Although the model is more conservative than its predecessor by favoring precision over recall, it reduces misclassification of nearby eclipsing binaries and other astrophysical false positives. Importantly, it appropriately lowers confidence in crowded fields where bright neighboring stars

are present, reflecting a desirable caution in ambiguous scenarios.

Applying the trained ensemble to unlabeled FFI TCEs produced a ranked catalog of candidates with associated uncertainty estimates, offering a valuable resource for prioritizing follow-up observations. This catalog expands the pool of vetted candidates beyond the 2-minute targets, supporting population studies and enabling the discovery of planets in regions of parameter space previously underexplored.

Future work will focus on optimizing the difference image branch through dedicated optimization and attention mechanisms, refining hyperparameters, and incorporating future sector data. These enhancements, together with the model’s ability to scale to large datasets, will help ensure that **ExoMiner++** remains a practical and effective tool for automated vetting in current and future transit surveys.

ACKNOWLEDGMENTS

MM and HV are supported through TESS XRP 2022 contract 22-XRP22-2-0173, NASA Academic Mission Services (NAMS) contract number NNA16BD14C as well as the Intelligent Systems Research and Development-3 (ISRDS-3) Contract 80ARC020D00100. DC, JT, MJ, and BT are supported through NASA Cooperative Agreement 80NSSC21M0079.

Resources supporting this work were provided by the NASA High-End Computing (HEC) Program through the NASA Advanced Supercomputing (NAS) Division at Ames Research Center for the production of the Kepler SOC and the TESS SPOC data products and for training

our deep learning model and preprocessing the data to be ingested by the model.

Funding for the TESS mission is provided by NASA’s Science Mission Directorate. This paper made use of data collected by the TESS mission and are publicly available from the Mikulski Archive for Space Telescopes (MAST) operated by the Space Telescope Science Institute (STScI). We acknowledge the use of public TESS data from pipelines at the TESS Science Office and at the TESS Science Processing Operations Center. This research has made use of the Exoplanet Follow-up Observation Program (ExoFOP; DOI: 10.26134/ExoFOP5) website, which is operated by the California Institute of Technology, under contract with the National Aeronautics and Space Administration under the Exoplanet Exploration Program. We would like to thank ExoFOP-TESS for hosting and sharing vetted TOI information and follow-up results, and the TESS Science Office and the TFOP SG1 Working Group, led by Dr. Karen A. Collins (CfA/SAO), for their vetting and ground-based follow-up of TESS Objects of Interest.

This material is based upon work supported by the NASA under Agreement No. 80NSSC21K0593 for the program “Alien Earths”. The results reported herein benefited from collaborations and/or information exchange within NASA’s Nexus for Exoplanet System Science (NExSS) research coordination network sponsored by NASA’s Science Mission Directorate.

We would also like to acknowledge the use of Microsoft Enterprise Copilot ([Microsoft 2025](#)), an AI-powered writing assistant, in editing portions of this manuscript to improve clarity and writing quality.

REFERENCES

Ansdell, M., Ioannou, Y., Osborn, H. P., et al. 2018, *The Astrophysical Journal*, 869, L7, doi: [10.3847/2041-8213/aaf23b](https://doi.org/10.3847/2041-8213/aaf23b)

Armstrong, D. J., Gamper, J., & Damoulas, T. 2020, *Monthly Notices of the Royal Astronomical Society*, 504, 5327–5344, doi: [10.1093/mnras/staa2498](https://doi.org/10.1093/mnras/staa2498)

Ba, J. L., Kiros, J. R., & Hinton, G. E. 2016, arXiv preprint arXiv:1607.06450

Borucki, W. J., Koch, D., Basri, G., et al. 2010, *Science*, 327, 977

Burke, C. J., Coughlin, J., Mullaly, S., et al. 2020, TESS-ExoClass. <https://github.com/christopherburke/TESS-ExoClass>

Caldwell, D. A., Tenenbaum, P., Twicken, J. D., et al. 2020, *Research Notes of the AAS*, 4, 201

Coughlin, J. L., Mullally, F., Thompson, S. E., et al. 2016, *The Astrophysical Journal Supplement Series*, 224, 12, doi: [10.3847/0067-0049/224/1/12](https://doi.org/10.3847/0067-0049/224/1/12)

Dietterich, T. G. 1998, *Neural computation*, 10, 1895

Efron, B., & Tibshirani, R. J. 1994, *An introduction to the bootstrap* (Chapman and Hall/CRC)

Eisner, N. L., Barragán, O., Lintott, C., et al. 2021, *Monthly Notices of the Royal Astronomical Society*, 501, 4669

Fukushima, K. 1969, *IEEE Transactions on Systems Science and Cybernetics*, 5, 322

Gaia Collaboration, Brown, A. G. A., Vallenari, A., et al. 2018, *A&A*, 616, A1, doi: [10.1051/0004-6361/201833051](https://doi.org/10.1051/0004-6361/201833051)

Giacalone, S., Dressing, C. D., Jensen, E. L. N., et al. 2020, *The Astronomical Journal*, 161, 24, doi: [10.3847/1538-3881/abc6af](https://doi.org/10.3847/1538-3881/abc6af)

Glorot, X., & Bengio, Y. 2010, in Proceedings of the thirteenth international conference on artificial intelligence and statistics, JMLR Workshop and Conference Proceedings, 249–256

Green, J., Schechter, P., Baltay, C., et al. 2012, arXiv preprint arXiv:1208.4012

Guerrero, N. M., Seager, S., Huang, C. X., et al. 2021, ApJS, 254, 39, doi: [10.3847/1538-4365/abefc1](https://doi.org/10.3847/1538-4365/abefc1)

He, K., Zhang, X., Ren, S., & Sun, J. 2015, in Proceedings of the IEEE international conference on computer vision, 1026–1034

He, K., Zhang, X., Ren, S., & Sun, J. 2016, in Proceedings of the IEEE conference on computer vision and pattern recognition, 770–778

Huang, C. X., Vanderburg, A., Pál, A., et al. 2020a, Research Notes of the American Astronomical Society, 4, 204, doi: [10.3847/2515-5172/abca2e](https://doi.org/10.3847/2515-5172/abca2e)

—. 2020b, Research Notes of the American Astronomical Society, 4, 206, doi: [10.3847/2515-5172/abca2d](https://doi.org/10.3847/2515-5172/abca2d)

Ioffe, S., & Szegedy, C. 2015, in International conference on machine learning, pmlr, 448–456

Jenkins, J. M., McCauliff, S., Burke, C., et al. 2014, in Formation, Detection, and Characterization of Extrasolar Habitable Planets, ed. N. Haghhipour, Vol. 293, 94–99, doi: [10.1017/S1743921313012611](https://doi.org/10.1017/S1743921313012611)

Jenkins, J. M., Twicken, J. D., McCauliff, S., et al. 2016, in Society of Photo-Optical Instrumentation Engineers (SPIE) Conference Series, Vol. 9913, Software and Cyberinfrastructure for Astronomy IV, ed. G. Chiozzi & J. C. Guzman, 99133E, doi: [10.1117/12.2233418](https://doi.org/10.1117/12.2233418)

Kingma, D. P. 2014, arXiv preprint arXiv:1412.6980

Kostov, V. B., Powell, B. P., Fornear, A. U., et al. 2025, ApJS, 279, 50, doi: [10.3847/1538-4365/ade2d8](https://doi.org/10.3847/1538-4365/ade2d8)

Li, J., Tenenbaum, P., Twicken, J. D., et al. 2019, Publications of the Astronomical Society of the Pacific, 131, 024506, doi: [10.1088/1538-3873/aaf44d](https://doi.org/10.1088/1538-3873/aaf44d)

Lindegren, L. 2018, http://www.rssd.esa.int/doc_fetch.php?id=3757412

Martinho, M., & Valizadegan, H. 2025, Vetting TESS Full-Frame Image Transit Signals with ExoMiner, 2.0.0, Zenodo, doi: [10.5281/zenodo.17707413](https://doi.org/10.5281/zenodo.17707413)

McCauliff, S. D., Jenkins, J. M., Catanzarite, J., et al. 2015, The Astrophysical Journal, 806, 6, doi: [10.1088/0004-637x/806/1/6](https://doi.org/10.1088/0004-637x/806/1/6)

Microsoft. 2025, Microsoft Copilot [AI Assistant], <https://copilot.microsoft.com>

Morton, T. D. 2012, The Astrophysical Journal, 761, 6, doi: [10.1088/0004-637x/761/1/6](https://doi.org/10.1088/0004-637x/761/1/6)

Morton, T. D., Bryson, S. T., Coughlin, J. L., et al. 2016, The Astrophysical Journal, 822, 86, doi: [10.3847/0004-637x/822/2/86](https://doi.org/10.3847/0004-637x/822/2/86)

Morton, T. D., & Johnson, J. A. 2011, The Astrophysical Journal, 738, 170, doi: [10.1088/0004-637x/738/2/170](https://doi.org/10.1088/0004-637x/738/2/170)

Nadeau, C., & Bengio, Y. 1999, Advances in neural information processing systems, 12

Prša, A., Kochoska, A., Conroy, K. E., et al. 2022, The Astrophysical Journal Supplement Series, 258, 16, doi: [10.3847/1538-4365/ac324a](https://doi.org/10.3847/1538-4365/ac324a)

Rauer, H., Catala, C., et al. 2010, Proceedings of the International Astronomical Union, 6, 354

Redmon, J., Divvala, S., Girshick, R., & Farhadi, A. 2016, in Proceedings of the IEEE conference on computer vision and pattern recognition, 779–788

Ricker, G. R., Winn, J. N., Vanderspek, R., et al. 2015, Journal of Astronomical Telescopes, Instruments, and Systems, 1, 014003, doi: [10.1117/1.JATIS.1.1.014003](https://doi.org/10.1117/1.JATIS.1.1.014003)

Shallue, C. J., & Vanderburg, A. 2018, The Astronomical Journal, 155, 94

Smith, J. C., Stumpe, M. C., Van Cleve, J. E., et al. 2012, PASP, 124, 1000, doi: [10.1086/667697](https://doi.org/10.1086/667697)

Stassun, K. G., Oelkers, R. J., Paegert, M., et al. 2019, AJ, 158, 138, doi: [10.3847/1538-3881/ab3467](https://doi.org/10.3847/1538-3881/ab3467)

Stumpe, M. C., Smith, J. C., Catanzarite, J. H., et al. 2014, PASP, 126, 100, doi: [10.1086/674989](https://doi.org/10.1086/674989)

Stumpe, M. C., Smith, J. C., Van Cleve, J. E., et al. 2012, PASP, 124, 985, doi: [10.1086/667698](https://doi.org/10.1086/667698)

Szegedy, C., Liu, W., Jia, Y., et al. 2015, in Proceedings of the IEEE conference on computer vision and pattern recognition, 1–9

Tey, E., Moldovan, D., Kunimoto, M., et al. 2023, The Astronomical Journal, 165, 95, doi: [10.3847/1538-3881/acad85](https://doi.org/10.3847/1538-3881/acad85)

Twicken, J. D., Catanzarite, J. H., Clarke, B. D., et al. 2018, Publications of the Astronomical Society of the Pacific, 130, 064502, doi: [10.1088/1538-3873/aab694](https://doi.org/10.1088/1538-3873/aab694)

Twicken, J. D., Caldwell, D. A., Jenkins, J. M., et al. 2020, TESS Science Data Products Description Document EXP-TESS-ARC-ICD-0014 Rev F, NASA/TM 20205008729, NASA Ames Research Center, <https://archive.stsci.edu/missions/tess/doc/EXP-TESS-ARC-ICD-TM-0014-Rev-F.pdf>

Valizadegan, H., Martinho, M. J. S., Jenkins, J. M., et al. 2023, The Astronomical Journal, 166, 28, doi: [10.3847/1538-3881/acd344](https://doi.org/10.3847/1538-3881/acd344)

Valizadegan, H., Martinho, M. J. S., Wilkens, L. S., et al. 2022, The Astrophysical Journal, 926, 120, doi: [10.3847/1538-4357/ac4399](https://doi.org/10.3847/1538-4357/ac4399)

Valizadegan, H., Martinho, M. J. S., Jenkins, J. M., et al. 2025, The Astronomical Journal, 170, 287,
doi: [10.3847/1538-3881/ae03a4](https://doi.org/10.3847/1538-3881/ae03a4)

Woo, S., Park, J., Lee, J.-Y., & Kweon, I. S. 2018, in Proceedings of the European conference on computer vision (ECCV), 3–19

Yu, L., Vanderburg, A., Huang, C., et al. 2019, The Astronomical Journal, 158, 25

Zhuang, F., Qi, Z., Duan, K., et al. 2020, Proceedings of the IEEE, 109, 43

APPENDIX

A. DETAILS OF ARCHITECTURE FOR **ExoMiner++** 2.0

We provide in detail the architecture and optimization parameters of **ExoMiner++** 2.0:

- All convolutional layers use a stride of 1, and their weights are initialized randomly following He initialization (He et al. 2015).
- All convolutional layers use ‘same’ padding (i.e., the feature map size is preserved), except for the first layer in each convolutional block, whose padding was set to ‘valid’ (thus downsampling the feature map similar to pooling). The only exception is the ‘Difference Image’ branch, whose convolutional layers all apply ‘same’ padding.
- All convolutional and FC layers are followed by a parametric rectified linear unit activation (Fukushima 1969, pReLU).
- All skip connections apply a convolutional layer with the same number of kernels, type of padding, and kernel size and stride as the first convolutional layer in each convolutional block so the feature map dimensions match. The kernel is initialized so the convolutional layer works initially as an identity layer.
- All layer normalization layers use $\epsilon = 1e-3$, with center and scale parameters initialized to ‘zeros’ and ‘ones’, respectively.
- All batch normalization layers use $\mu = 0.99$ and $\epsilon = 1e-3$, with center and scale parameters initialized to ‘zeros’ and ‘ones’, respectively.
- All FC layers in the classification head apply a dropout with rate of $2.15e-2$, and their weights are initialized randomly following Glorot uniform initialization (Glorot & Bengio 2010).
- Batch size was set to 256 to provide stable statistics for batch normalization.
- Learning rate was set to $4.18e-5$ to compensate batch size increase.